

THE IONIZED GAS AND NUCLEAR ENVIRONMENT IN NGC 3783. IV. VARIABILITY AND MODELING OF THE 900 KILOSECOND *CHANDRA* SPECTRUM

HAGAI NETZER,¹ SHAI KASPI,¹ EHUD BEHAR,² W. N. BRANDT,³ DORON CHELOUCHE,¹ IAN M. GEORGE,^{4,5}
 D. MICHAEL CRENSHAW,⁶ JACK R. GABEL,⁷ FREDERICK W. HAMANN,⁸ STEVEN B. KRAEMER,⁷
 GERARD A. KRISS,^{9,10} KIRPAL NANDRA,¹¹ BRADLEY M. PETERSON,¹²
 JOSEPH C. SHIELDS,¹³ AND T. J. TURNER^{4,5}

Received 2003 July 7; accepted 2003 September 2

ABSTRACT

We present a detailed spectral analysis of the data obtained from NGC 3783 during the period 2000–2001 using *Chandra*. The data were split in various ways to look for time- and luminosity-dependent spectral variations. This analysis, along with the measured equivalent widths of a large number of X-ray lines and photoionization calculations, lead us to the following results and conclusions. (1) NGC 3783 fluctuated in luminosity by a factor of ~ 1.5 during individual observations (most of which were of 170 ks duration). These fluctuations were not associated with significant spectral variations. (2) On a longer timescale (20–120 days), we found the source to exhibit two very different spectral shapes. The main difference between these can be well-described by the appearance (in the “high state”) and disappearance (in the “low state”) of a spectral component that dominates the underlying continuum at the longest wavelengths. Contrary to the case in other objects, the spectral variations are not related to the brightening or the fading of the continuum at short wavelengths in any simple way. NGC 3783 seems to be the first active galactic nucleus (AGN) to show this unusual behavior. (3) The appearance of the soft continuum component is consistent with being *the only* spectral variation, and there is no need to invoke changes in the opacity of the absorbers lying along the line of sight. Indeed, we find that all the absorption lines that can be reliably measured have the same equivalent widths (within the observational uncertainties) during high and low states. (4) Photoionization modeling indicates that a combination of three ionized absorbers, each split into two kinematic components, can explain the strengths of almost all the absorption lines and bound-free edges. These three components span a large range of ionization and have total column of about $4 \times 10^{22} \text{ cm}^{-2}$. Moreover, all three components are thermally stable and seem to have the same gas pressure. Thus, all three may coexist in the same volume of space. This is the first detection of such a multicomponent, equilibrium gas in an AGN. (5) The only real discrepancy between our model and the observations concerns the range of wavelengths absorbed by the iron M-shell UTA feature. This most likely arises as the result of our underestimation of the poorly known dielectronic recombination rates appropriate for these ions. We also note a small discrepancy in the calculated column density of O VI and discuss its possible origin. (6) The lower limit on the distance of the absorbing gas in NGC 3783 is between 0.2 and 3.2 pc, depending on the component of ionized gas considered. The assumption of pressure equilibrium imposes an upper limit of about 25 pc on the distance of the least-ionized component from the central source.

Subject headings: galaxies: active — galaxies: individual (NGC 3783) — galaxies: nuclei — galaxies: Seyfert — techniques: spectroscopic — X-rays: galaxies

1. INTRODUCTION

The barred spiral galaxy NGC 3783 ($V \simeq 13.5$ mag, $z = 0.0097$) hosts a well-studied, type I active galactic nucleus (AGN) with prominent broad emission lines and strong X-ray absorption features. The object has been observed extensively with almost all X-ray instruments,

most recently by *Chandra* (Kaspi et al. 2002, hereafter Paper I) and *XMM-Newton* (Blustin et al. 2002). The 2–10 keV flux of NGC 3783 varies in the range $\sim (4\text{--}9) \times 10^{-11} \text{ ergs cm}^{-2} \text{ s}^{-1}$, and its mean 2–10 keV luminosity is $\sim 1.5 \times 10^{43} \text{ ergs s}^{-1}$ (for $H_0 = 70 \text{ km s}^{-1} \text{ Mpc}^{-1}$ and $q_0 = 0.5$). Paper I gives an extensive list of references and a comprehensive summary of historical observations,

¹ School of Physics and Astronomy, Raymond and Beverly Sackler Faculty of Exact Sciences, Tel-Aviv University, Tel-Aviv 69978, Israel.

² Physics Department, Technion, Haifa 32000, Israel.

³ Department of Astronomy and Astrophysics, 525 Davey Laboratory, Pennsylvania State University, University Park, PA 16802.

⁴ Laboratory for High Energy Astrophysics, NASA Goddard Space Flight Center, Code 662, Greenbelt, MD 20771.

⁵ Joint Center for Astrophysics, Physics Department, University of Maryland, Baltimore County, 1000 Hilltop Circle, Baltimore, MD 21250.

⁶ Department of Physics and Astronomy, Georgia State University, Atlanta, GA 30303.

⁷ Catholic University of America, NASA Goddard Space Flight Center, Code 681, Greenbelt, MD 20771.

⁸ Department of Astronomy, University of Florida, 211 Bryant Space Science Center, Gainesville, FL 32611-2055.

⁹ Center for Astrophysical Sciences, Department of Physics and Astronomy, Johns Hopkins University, Baltimore, MD 21218-2686.

¹⁰ Space Telescope Science Institute, 3700 San Martin Drive, Baltimore, MD 21218.

¹¹ Astrophysics Group, Imperial College London, Blackett Laboratory, Prince Consort Road, London SW7 2AZ, UK.

¹² Department of Astronomy, Ohio State University, 140 West 18th Avenue, Columbus, OH 43210-1106.

¹³ Department of Physics and Astronomy, Clipping Research Labs 251B, Ohio University, Athens, OH 45701-2979.

including ground-based and UV *Hubble Space Telescope* (*HST*) observations. It also discusses the unique *Chandra* data set obtained in 2000–2001. These observations consist of a relatively short observation performed in 2000 January and five longer observations performed in 2001 February–June, separated by various intervals from 2 to 120 days (see § 2). Paper I contains numerous illustrations of the mean spectrum, absorption line profiles, and detailed measurements of many absorption and emission lines. Two other papers (Gabel et al. 2003a, 2003b) discuss the *HST* and *Far Ultraviolet Spectroscopic Explorer* (*FUSE*) data obtained as part of this multiwaveband campaign.

There have been several previous attempts to model the characteristics of the X-ray-absorbing gas along the line of sight to NGC 3738. Here we comment only on the more detailed works. A very detailed work by Kaspi et al. (2001) attempted to fit the spectrum obtained with *Chandra* in 2000. The Kaspi et al. most successful model consists of two absorbing shells, both outflowing from the central source with a velocity of $\sim 600 \text{ km s}^{-1}$. The gas in both shells was assumed to be turbulent with internal turbulent motion of $\sim 250 \text{ km s}^{-1}$. The two shells had similar column densities but different ionization parameters. The model is consistent with the intensity and equivalent width (EW) of many (but not all) emission and absorption lines observed in the spectrum. A major limitation of the Kaspi et al. (2001) work was the limited signal-to-noise ratio (S/N) of the spectrum, which results in large uncertainties on the model parameters. In addition, the limited duration of the only observation then available did not allow a meaningful analysis of any time dependence. A new paper by Krongold et al. (2003, hereafter K03) discussing the full *Chandra* data set was accepted for publication after the submission of our paper. Some results of that work are relevant to our study and are discussed in the various sections below.

This paper discusses the complete spectroscopic *Chandra* data of NGC 3738. We present our modeling of this material, with emphasis on the properties of the absorber(s) along the line of sight. In § 2 we describe the two X-ray spectral states discovered using the new observations. In § 3 we explain the various ways we measured and modeled the spectrum. Section 4 contains a discussion of the new findings, and § 5 summarizes our new results.

2. THE TWO-STATE X-RAY SPECTRUM OF NGC 3738

A full description of the *Chandra* data considered here is given in Paper I. In brief, there were five observations (of ~ 170 ks duration each) obtained over the period 2001 February–June and a shorter observation (of ~ 56 ks duration) obtained in 2000 January (and also discussed in Kaspi et al. 2001). All six observations were performed with the High-Energy Transmission Grating Spectrometer (HETGS) in place and consist of a total exposure of 888.7 ks. All measurements in Paper I refer to a time-averaged spectrum, produced by combining the first-order spectra from both grating arms, using 0.01 Å wide bins. Third-order data from the medium-energy grating (MEG) were also used to compare the profiles of several short-wavelength lines with the first-order profiles obtained for several lines at longer wavelength. It was found that most of the resolved absorption lines (e.g., O VII, Ne IX, and Si XIV lines) consist of at least two kinematic components, outflowing at -500 ± 100 and $-1000 \pm 200 \text{ km s}^{-1}$, respectively. The

overall absorption profiles in NGC 3738 cover the velocity range of 0 to -1600 km s^{-1} (e.g., see Paper I, Figs. 5 and 10).

A major goal of the present work is to investigate subsets of the *Chandra* data. We subdivided the data in various ways to search for spectral variations as a function of source luminosity and/or time. This was done for both short (i.e., within the individual 170 ks observations) as well as for long (between observations, i.e., 20–90 days) timescales. The short timescale behavior of NGC 3738 is illustrated in Figure 1, which shows the short wavelength ($2\text{--}10 \text{ Å}$) flux as a function of time for all observations binned in intervals of 3170 s in the left panels. The right panels show the “softness” ratio, defined as the flux in the $15\text{--}25 \text{ Å}$ band divided by that in the $2\text{--}10 \text{ Å}$ band to illustrate now the different variability characteristics exhibited by the source above and below $\sim 1 \text{ keV}$.

From Figure 1, it can be seen that the $2\text{--}10 \text{ Å}$ flux varied by about 50% over the 170 ks duration of each of the observations. However, inspection of the corresponding softness light curves shows that the spectral variations are much smaller and almost insignificant. Thus, the data show very little change of the spectral energy distribution (SED) over timescales $\lesssim 4$ days (observation IDs 2090 and 2091 are consecutive with total duration of about 4 days). To further test this finding, we also extracted various spectra when the source was in different intensity states but did not find any significant spectral variations during this period. We also note that Behar et al. (2003) did not find any spectral variations during a three-day observation of NGC 3738 in 2001 December using *XMM-Newton*.

Contrary to the above, there is a *very significant* change of SED on longer timescales. In particular, there is a major change in the softness ratio between obsIDs 2092 and 2093 (separated by 20 days) and obsIDs 2093 and 2094 (separated by 90 days). As shown in Figure 1, obsID 2093 shows a higher mean count rate but exhibits a much softer spectrum. Direct comparison of the time-averaged spectra obtained during obsID 2093 with that obtained during obsID 2094 reveals the low-energy part ($\lambda > 15 \text{ Å}$) decreased in flux by a factor of ~ 4 , but that the shorter wavelength continuum exhibited a much smaller decrease (factor of ~ 1.5). The opposite change occurred between obsIDs 2092 and 2093. Most importantly, the softness ratio variations *are not* simple luminosity-related effects. For example, the $2\text{--}10 \text{ Å}$ count rate in the middle of obsID 2093 (Fig. 1) is a little lower than the $2\text{--}10 \text{ Å}$ flux toward the end of obsID 2094, yet the softness ratios are significantly different. A similar effect is seen in obsID 2093, during which the $2\text{--}10 \text{ Å}$ count rate varied by about 50%, yet the softness ratio remained approximately constant.

In light of these results, we have divided the entire data set into groups with high and low softness ratios. We find four observations (2090, 2091, 2092, and 2094) with low softness ratios and two (0373 and 2093) with high softness ratios. Hereafter, we refer to these as the “low-” and “high-state” observations, respectively. We find no significant differences between the mean spectra of the four individual low-state observations (except for a small intensity variations). Similarly, we find no significant differences between the mean spectral shapes of the two high-state observations.

Figure 2 is a more detailed example of this phenomenon. It shows the softness ratio as a function of the $2\text{--}10 \text{ Å}$ flux for all the data using 3170 s bins. A separation into two groups is apparent, and a standard K-S statistical test

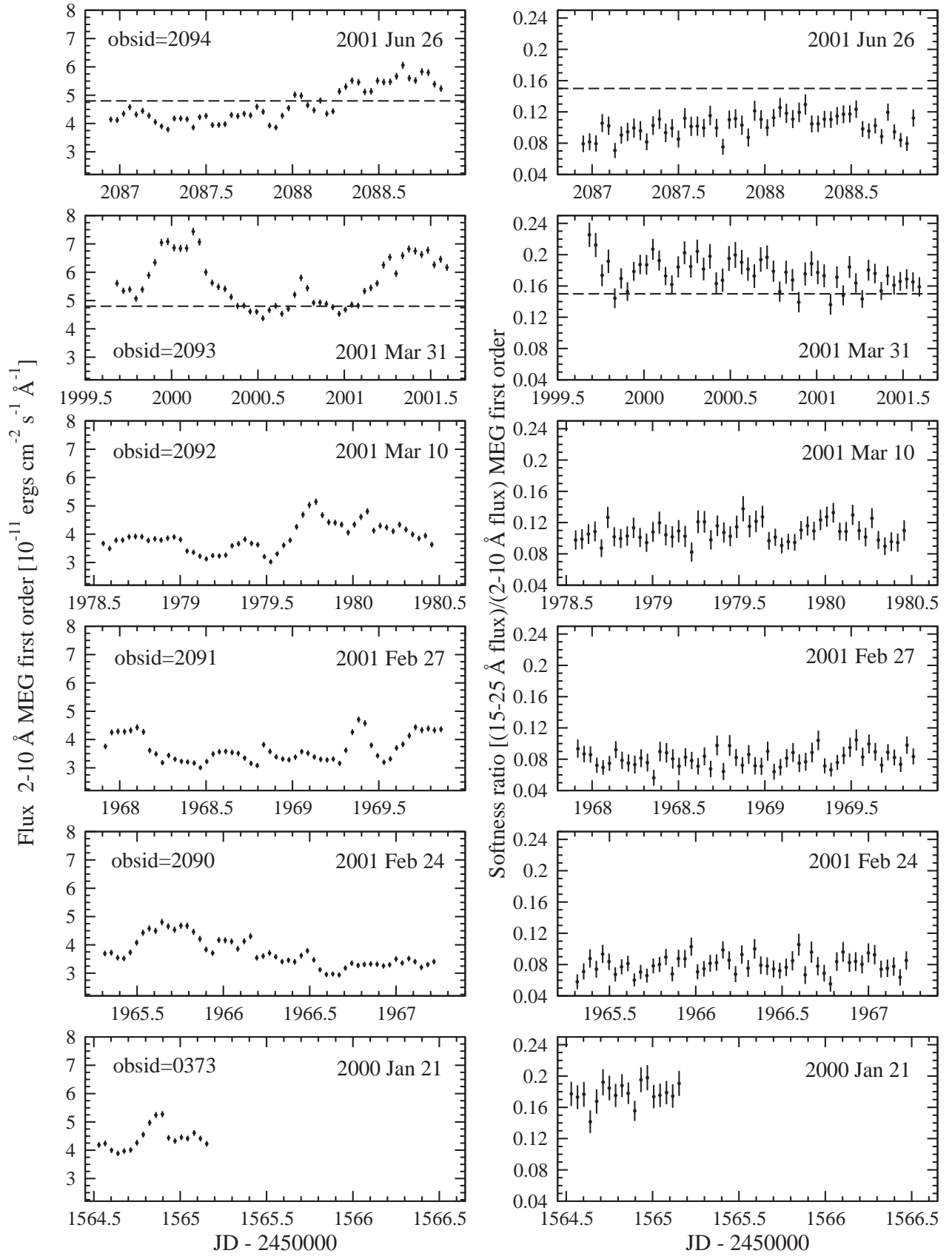


FIG. 1.—MEG 2–10 Å flux light curves (left) and softness ratios (ratio of the 2–10 and the 15–25 Å count rates; right) for all *Chandra* observations of NGC 3783. Dashed lines across observations 2093 and 2094: Constant flux (4.8) and softness ratio (0.15). They illustrate the fact that similar 2–10 Å fluxes (middle part of observation 2093 and last part of 2094) can be associated with very different softness ratios.

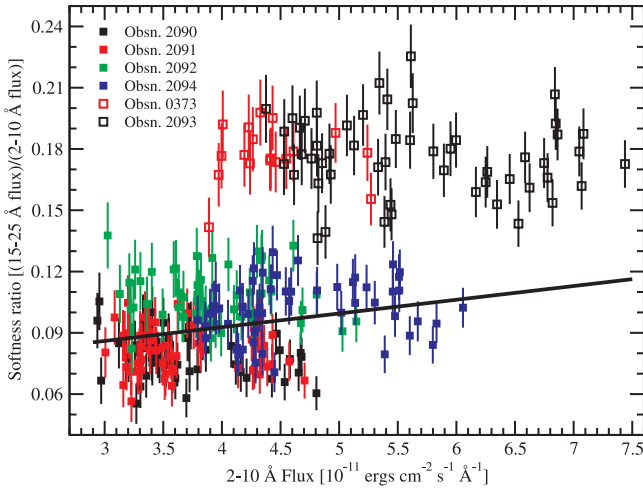


FIG. 2.—Softness ratio vs. 2–10 Å flux for the data in Fig. 1. The low- and high-state observations are shown as filled and open symbols, respectively, and the various observations are denoted with different colors. *Solid straight line*: Linear regression fit to the low-state observations. No significant correlation of softness ratio vs. flux was found for the high-state observations.

confirms its significance. We have also investigated possible linear correlations of the softness ratio with the 2–10 Å flux within each of the states. For the low-state observations, we find a significant ($>99\%$) linear correlation between softness ratio and flux. However, as can be seen from Figure 2, this line clearly does not connect the low- and high-state data. No significant correlation of softness ratio with flux was found for the high-state data. We conclude that the X-ray spectrum of NGC 3783 fluctuates between two states of different softness ratios. The combined spectra of the two are shown in Figure 3, and much of the rest of this paper is devoted to the analysis of this unusual behavior of NGC 3783.

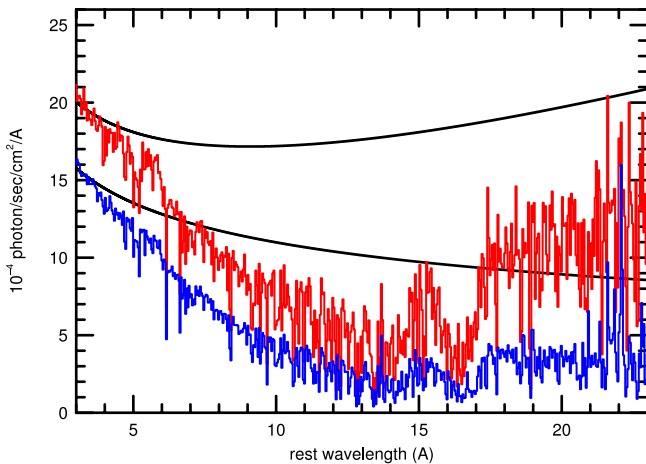


FIG. 3.—High-state (red; observations 0373 and 2093 combined) and low-state (blue; all other observations combined) spectra of NGC 3783 binned to 0.04 Å. *Solid lines*: Two chosen intrinsic continua (see § 3.2.5). The lower continuum is a single power law with $\Gamma = 1.6$. The high continuum is made out of two power laws with slopes $\Gamma = 1.6$ and 3.2 and relative normalization of 1 : 0.4 at 1 keV. These power laws are discussed in § 3.2.5.

3. SPECTRAL ANALYSIS AND MODELING

3.1. Spectral Differences between the High and Low States

We have investigated the unusual variations observed in the spectrum of NGC 3783 in an attempt to understand their nature and their origin. In particular, we have attempted to answer the question of whether they are due to the response of the absorbing gas to the variations observed in the continuum.

There are two ways to answer the above question: by a direct and detailed spectral comparison and by modeling the two spectra, trying to establish the origin of the differences. Figure 4 is an example of the first approach. The diagrams shows a comparison of the low- and high-state spectra after applying a simple scaling factor to the former such that the (local) continua have the same intensity. As the scaling factor is wavelength dependent, we divided the two spectra into several bands and applied different factors in each case. The two examples shown in Figure 4 (and all others we have examined) illustrate that, except for a luminosity scaling, the two absorption-line spectra are indistinguishable within the uncertainties ($\sim 10\%$ for the low-state spectrum and about twice that for the high-state spectrum). The somewhat weaker looking lines of low-ionization species in the high-state spectrum (e.g., around 7 Å) are well within the noise. Table 1 lists the EWs measured for several key absorption lines (see § 3.2.3) in both the high- and low-state spectra. Again, the small differences between the two spectra are well within the measurement errors. We proceed under the assumption that there are no variations in the line EWs between the two states. We comment on the implications of this in § 4.1.

3.2. Spectral Modeling

The second and complementary approach for investigating the spectral changes is by detailed modeling of the absorbing and emitting gas. The underlying idea is that the gas is photoionized by the central X-ray source and that the observed spectra represent its physical state during the two states. The principles and the ingredients of such modeling were outlined in Netzer (1996), and previous applications to the case of NGC 3783 were discussed by Kaspi et al. (2001). A very recent analysis is provided by K03, who describe a detailed model composed of two absorbers that are different from those suggested by Kaspi et al. (2001).

TABLE 1
EQUIVALENT WIDTHS^a

Ion and Line	Low State	High State	Kaspi et al. (2002)
Si xiv λ 6.182	20.4 ± 1.2	22.6 ± 1.7	20.5 ± 0.8
Si xiii λ 6.648	16.0 ± 1.3	14.6 ± 1.3	14.9 ± 0.7
Si xii λ 6.718 ^b	2.9 ± 0.5	3.8 ± 0.7	3.0 ± 0.4
Si xi λ 6.778	4.8 ± 0.8	5.9 ± 1.2	4.8 ± 0.6
Si x λ 6.859	10.6 ± 1.1	9.4 ± 1.4	10.9 ± 0.8
Si ix λ 6.931	7.2 ± 1.0	7.7 ± 1.6	7.1 ± 0.7
Si viii λ 6.999	4.3 ± 1.0	4.4 ± 1.4	4.3 ± 0.8
S xvi λ 4.729	11.5 ± 1.6	11.6 ± 2.5	10.7 ± 1.2
S xv λ 5.039	8.7 ± 1.7	9.1 ± 2.5	9.2 ± 1.2

^a Equivalent widths were measured as described in Paper I and are given in mÅ.

^b This line is blended with Mg xii λ 6.738 with 1 : 1 ratio. Tabulated values are only for the Si xii λ 6.718 line.

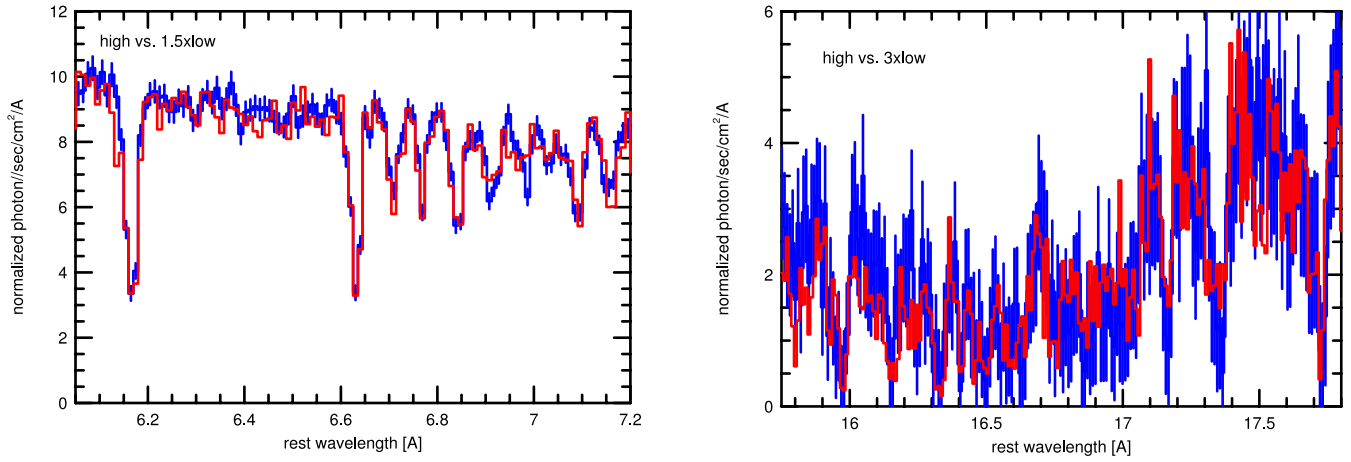


FIG. 4.—*Left*: High-state (red) vs. low-state (blue) 6–7 Å spectra of NGC 3783 showing the great similarity in absorption line EWs (cf. Table 1). The low-state spectrum was multiplied by 1.5 to match the flux of the high-state continuum. For clarity, error bars are only plotted for the low-state spectrum. *Right*: Same for the 15.6–18 Å range, except for the different scaling of the low-state continuum.

Below, we comment on the similarity and differences between our work and the new K03 paper. Here we summarize our basic method and explain its application to the high- and the low-state spectra of NGC 3783.

3.2.1. General Method and Model Ingredients

The X-ray gas is assumed to be photoionized by a central source and in photoionization and thermal equilibrium (see § 4 for discussion of the last point). Modeling was performed using ION2003, the 2003 version of the code ION (Netzer 1996). The code includes all relevant atomic processes and computes the ionization and thermal structure of the gas along with the intensities and EWs for more than 2000 X-ray lines. The code considers various geometries, from a single cloud to a multicomponent, expanding atmosphere. The basic parameters of the model are the gas density (assumed to be in the range 10^2 – 10^6 cm^{-3} ; see justification in § 4), the hydrogen column density (N , in units of cm^{-2}), the covering factor, the gas composition, turbulent motion (§ 3.2.2), and the oxygen ionization parameter (U_{ox}) defined over the energy range 0.54–10 keV. As explained by Netzer (1996) and discussed further in George et al. (1998), this choice of ionization parameter (compared with, e.g., U_X defined over the 0.1–10 keV range) gives the most meaningful definition of the ionization field of X-ray photons for AGNs. Regarding the covering factor, we distinguish between the emission covering factor ($\Omega/4\pi$) applicable to the emission line gas and the absorption (line-of-sight) covering factor, which can be different. The “solar composition” used throughout this work is given in Table 2 (note the reduced oxygen abundance compared with older estimates).

The incident continuum is taken to be the broken power law defined in Kaspi et al. (2001, Table 4). The only changes we have experimented with are related to the slope of the 0.1–50 keV continuum. As discussed below, the UV part of the spectrum can be different from the one assumed here with important implications for the UV absorption lines. This will be investigated in a forthcoming paper. The effects of the UV continuum on the strongest features seen in the X-ray band are of far less importance. Thus, we consider this SED to be adequate for the present analysis.

The models calculated here are entirely self-consistent and are not simple attempts to fit the observed spectra by measuring line EWs and deducing column densities for the different ions. We have searched for the combination of physical components that can be produced in nature in an environment where low-density gas is exposed to a typical AGN continuum. These components were then combined in a realistic manner, taking into account screening, attenuation of the radiation field, etc.

3.2.2. Multicomponent Models

We have examined the hypothesis that the spectral changes observed arise purely as a result of variations in the opacity of the absorbing gas, which are caused solely by changes in the intensity of the ionizing continuum. Thus, for this experiment, we assume the shape of the SEDs is the same for both the low and high states and only differ in total luminosity. We start by calculating a variety of models in order to mimic the low-state spectrum. Each model is made of several emission and absorption components. The absorbers are specified by U_{ox} , N , and the absorption (i.e., line-of-sight) covering factor. The latter is assumed to be the same for all absorbers (but see also § 4). The absorbers are

TABLE 2
ASSUMED COMPOSITION

Element	Relative Abundance
H	1.0
He	0.1
C	3.7×10^{-4}
N	1.1×10^{-4}
O	5.0×10^{-4}
Ne	1.0×10^{-4}
Mg	3.7×10^{-5}
Al	3.0×10^{-6}
Si	3.5×10^{-5}
S	1.6×10^{-5}
Ar	3.3×10^{-6}
Ca	2.3×10^{-6}
Fe	4.0×10^{-5}

assumed to be aligned such that the observed spectrum is the result of the intrinsic continuum passing through them all. The emission components are specified by their U_{ox} and N (not necessarily the same as those of the absorbers), their covering factor, and whether or not they are occulted by the absorbing gas.

The dynamics and kinematics of the absorbing gas are important factors in comparing the data with the model. Following numerous UV observations and our analysis in Paper I, we assumed internal motion in the gas that is much larger than the thermal motion. This “turbulent velocity” is assumed to have a Doppler profile, and the velocity quoted is the Doppler b parameter. Paper I showed that *all absorption lines* with good S/N and sufficient resolution (the lines of O VII, Ne X, Mg XII, and Si XIV) can be characterized by two kinematic components. The central velocities of these are between -400 and -600 km s $^{-1}$ and between -1000 and -1300 km s $^{-1}$, relative to the systemic velocity. A good representation of the observations can be obtained with two Doppler profiles, each with $b \simeq 250$ km s $^{-1}$.

The relative EW and covering factor of the two velocity components are critical to our modeling of the source. The observations show that the EW ratio of the velocity components is about 1:0.7 (lower:higher) in all lines with sufficient S/N (see below). Since this ratio is seen in several saturated lines, it can be interpreted as the result of different absorption covering factors for each component. In this case, the lower velocity component has a covering factor of 0.8–1.0 and the larger velocity component a covering factor of 0.6–0.8. However, the composite profiles also include unsaturated lines that seem to have similar shapes. In this case, the different EWs are due to different column densities. We cannot distinguish between the two possibilities since we do not have high-quality, high-resolution profiles for many weak lines. Given these uncertainties, we investigated two cases where the relative column densities for the two velocity components are in the ratio of 1:0.7. In one case, the covering factor of all absorbers is unity and in the other case it is of the order of 0.8.

In summary, each ionization component of the models presented in this paper is made of two kinematic components. For the outflow velocities, we chose -500 and -1000 km s $^{-1}$ and assumed a turbulent velocity of 250 km s $^{-1}$ for all components. This implies that the total derived column density of a certain ionization component is *the sum* of the column densities in the two kinematic components, even for saturated lines (since there is very little velocity overlap between the two). For brevity, in the rest of this paper, we just quote the total column densities. Given these assumptions, we used the EWs measured in Paper I, combined with a few new measurements, to obtain the various column densities and optical depths. The more important lines that were used to constrain our models, and their adopted column densities, are listed in Table 3.

3.2.3. The Silicon and Sulphur Line Method

A major clue for the conditions in the absorbing gas is obtained from EW measurements of various lines in the 5–7.1 Å band. This wavelength range contains lines from Si VII to Si XIV as well as the strongest lines of S XV and S XVI. Most of these lines are not blended. The range of ionization and excitation is very large and represents the ionization of almost all line-producing ions in the *Chandra* spectrum. The

column densities deduced from these EWs, assuming the two component profiles, are given in Tables 1 and 3. The atomic data for the lines are known either from standard calculations (f -values for the H-like and He-like transitions) or from the recent work of Behar & Netzer (2002) discussing the inner-shell lines of silicon, sulphur, and other elements.

We have developed a simple algorithm to compare the measured optical depths of all the observed silicon and sulphur lines with the results of the photoionization calculations. We first compute a large grid of models with calculated optical depths for a large range of ionization parameters and column densities. We then pick up to four models at a time and compare the *combined* optical depth for the chosen set of lines with the values deduced from the observations for the larger column density (lower outflow velocity) kinematic component. The best combination of models is obtained by minimizing the differences between the observed and the calculated optical depths in all 10 lines (the nine silicon and sulphur lines listed in Table 1 plus a line of Si VII). The result is a list of up to four models, with various column density and U_{ox} , whose combination gives the best match to the observed column densities. Using this procedure, we find that at least three ionization components (i.e., six kinematic components) are required to fit the data to within the observational accuracy. The reason is the very large difference in ionization between the lowest (e.g., Si VII and Si VIII) and the highest (e.g., S XVI) ionization lines. This requires at least one component to fit the EWs of the lowest ionization lines, one to fit the intermediate ionization lines, and one for the highest ionization lines.

Experimenting with various modifications of the method suggests that there are several combinations of three or four ionization components that give similar quality fits to the observed optical depths of the silicon and sulphur lines. All combinations share the same general properties—they all require at least three very different sets of physical conditions (i.e., ionization parameters) and three similar column densities. A generic model with the required properties is the following three-component model (all column densities refer to the total column of the two kinematic components): a low-ionization component with $\log(U_{\text{ox}}) = -2.4 \pm 0.1$ and $\log(N) = 21.9 \pm 0.1$, a medium-ionization component with $\log(U_{\text{ox}}) = -1.2 \pm 0.2$ and $\log(N) = 22.0 \pm 0.15$, and a high-ionization component with $\log(U_{\text{ox}}) = -0.6 \pm 0.2$ and $\log(N) = 22.3 \pm 0.2$. The uncertainties on U_{ox} and N in the case of the low-ionization component arise primarily from the uncertainty on the slope of the ionizing continuum. Relaxing this constraint allows a somewhat smaller column density (see § 3.2.4). The larger uncertainties on the parameters of the higher ionization components are due to the fact that gas with such properties produces similar EWs for medium- (e.g., Si XI) and high- (e.g., Si XIV) ionization lines over a larger range of ionization parameters and column densities. The three theoretical ionization components are plotted over a large wavelength range in Figure 5, and a more detailed view of the 4.5–7 Å range is shown in Figure 6.

3.2.4. Intrinsic Continuum and Global Model Properties

The next step is to test the combination of components that fit the optical depths of the 5–7.1 Å silicon and sulphur ions best over other wavelength bands. This requires the shape of the underlying ionizing continuum to be defined

TABLE 3
COLUMN DENSITIES^a

ION AND LINE	MEASURED ^b	MODEL $\log(U_{\text{ox}})$			
		−2.4	−1.2	−0.6	Total
Si XIV $\lambda 6.182$	>17.50 ^c
Si XIV $\lambda 5.217$	17.94 ± 0.10
Si XIV $\lambda 4.947$	17.83 ± 0.20
Si XIV adopted value	17.90 ± 0.20	12.50	17.00	17.48	17.60
Si XIII $\lambda 6.648$	>16.87 ^c
Si XIII $\lambda 5.681$	>17.23 ^c
Si XIII $\lambda 5.405$	17.57 ± 0.20
Si XIII $\lambda 5.286$	17.71 ± 0.25
Si XIII adopted value	17.65 ± 0.20	14.68	17.31	16.94	17.46
Si XII $\lambda 6.718$	16.10 ± 0.06	15.57	16.55	15.41	16.62
Si XI $\lambda 6.778$	16.29 ± 0.06	16.43	16.15	14.11	16.61
Si X $\lambda 6.859$	16.83 ± 0.05	16.90	15.88	13.10	16.94
Si IX $\lambda 6.931$	16.66 ± 0.06	17.04	15.27	11.68	17.05
Si VIII $\lambda 6.999$	16.66 ± 0.08	16.81	14.26	9.93	16.81
Si VII $\lambda 7.063$	16.26 ± 0.20	16.13	12.71	7.80	16.13
S XVI $\lambda 4.729$	>17.29 ^c
S XVI $\lambda 3.991$	17.58 ± 0.13
S XVI adopted value	17.58 ± 0.13	10.13	16.23	17.16	17.21
S XV $\lambda 5.039$	16.87 ± 0.09
S XV $\lambda 4.299$	17.08 ± 0.25
S XV adopted value	17.00 ± 0.20	12.70	16.90	17.00	17.25
Mg VIII $\lambda 9.506$	16.58 ± 0.05	16.77	14.46	11.13	16.77
Mg IX $\lambda 9.378$	16.39 ± 0.06	17.06	15.13	12.61	17.07
O VIII $\lambda 14.821$	18.67 ± 0.25
O VIII $\lambda 14.634$	18.59 ± 0.14
O VIII adopted value	18.63 ± 0.25	17.65	18.05	17.55	18.28
O VII $\lambda 17.396$	18.03 ± 0.20
O VII $\lambda 17.200$	18.04 ± 0.20
O VII adopted value	18.04 ± 0.20	18.39	16.84	15.49	18.40
O VI $\lambda 21.01$	>16.42 ^c
O VI $\lambda 19.341$	>17.00 ^c
O VI adopted value	>17.00	17.96	14.34	12.23	17.96
O V $\lambda 22.334$	>16.34 ^c
O V $\lambda 19.924$	17.07 ± 0.40
O V adopted value	17.07 ± 0.40	17.54	12.59	9.3	17.54

^a Log of column density in units of cm^{-2} .

^b Column densities and uncertainties derived from the EWs in Paper I. The EW was divided in the ratio 1:0.7, then the column density corresponding to the 1/1.7 part was computed assuming a Doppler width of 250 km s^{-1} . The derived column density was multiplied by 1.7 to result with the total column density listed here. Uncertainties were calculated from the EW uncertainties. See text for details.

^c Saturated line, lower limit only.

more precisely. The slope of the short wavelength continuum can be measured directly if bound-free absorption is negligible. However, Figure 5 clearly shows that two of the generic absorbers are characterized by large opacity at wavelengths as short as 4–5 Å. Thus, a unique determination of the 2–5 Å continuum slope (the part available for the grating observations) is not trivial. More specifically, the exact O VII column density in the lowest ionization component strongly influences the short-wavelength continuum shape, and the uncertainty on this column gives rise to an uncertainty on the slope.

Given the above constraints on the model properties and the observed 2–5 Å continuum, we have experimented with various power-law continua with the requirement that both the short wavelength continuum and the measured EWs of the silicon and sulphur lines, are within the observational uncertainties. All fits were performed on the low-state spectrum. We found that a single power law (where the number

of photons per unit energy, E , is proportional to $E^{-\Gamma}$) with $\Gamma = 1.65 \pm 0.15$ is a good overall representation of the low-state spectrum. We note that the limited data quality cannot exclude the possibility of some steepening of the intrinsic continuum at long ($\lambda > 20 \text{ Å}$) wavelengths.

We note in passing the different continuum slope adopted by K03 in their recent modeling of the source. These authors did not consider the two spectral states found here and fitted the full *Chandra* data set. As a result, the SED they adopted is based on the combined (high- and low-state) spectrum, and hence, is different from ours. This is also the reason that their power-law slope is flatter than the one adopted by Kaspi et al. (2001), who fitted the high state only. K03 also include in their SED a low-energy blackbody component.

Another uncertainty on the intrinsic SED arises from the fact that some of the high-energy photons are likely to be produced far away from the source because of Compton scattering and reflection of the central continuum radiation.

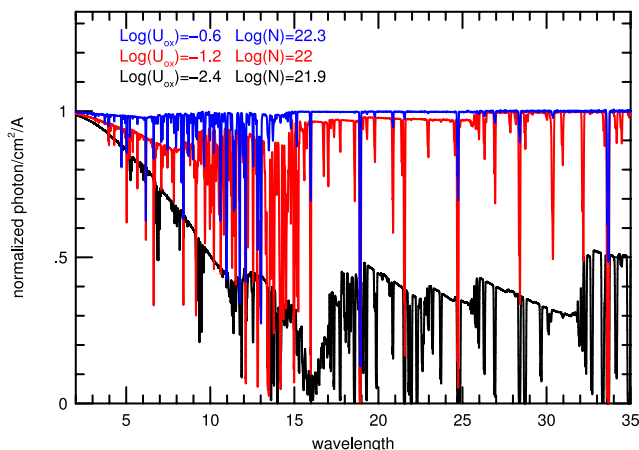


FIG. 5.—Three generic components that were used to model the low-state spectrum of NGC 3783. All components are shown on the same normalized scale, where 1 is the incident continuum level.

This can be very noticeable in faint sources, such as NGC 3516 during 2000 (see Netzer et al. 2002). Scattering by gas in a low state of ionization is strongly wavelength dependent, and for NGC 3783, can amount to a change of ~ 0.1 in the derived value of Γ . As a result, we might have overestimated the column density of the lowest ionization component (the only component with significant influence on the slope of the short wavelength continuum), which would result in overestimating the column densities of low ionization species such as O v and O vi. Section 4.1 contains some discussion about the lowering of the column density in our low- U_{ox} component, and a more detailed examination of this effect is deferred to a separate paper (I. M. George et al. 2003, in preparation).

Finally, a broad, relativistic iron $K\alpha$ line can also be important in affecting the short wavelength continuum slope. The presence or absence of such a feature is an open question. Kaspi et al. (2001) see no evidence for this feature in the 2000 *Chandra* observation. Given the uncertainties discussed above and the large amount of absorption at

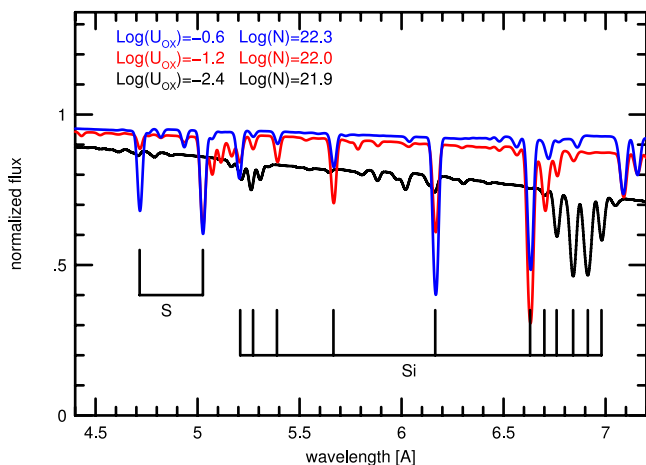


FIG. 6.—Enlarged version of Fig. 5 showing the 4.5–7 Å region used to constrain the model parameters (see text). Note that all three models are required to explain the large range of ionization (from Si vii to S xvi.)

almost all wavelengths, we cannot resolve this issue even with our much improved data.

Given the chosen continuum and the three ionization components, we have calculated a combined multicomponent model that covers the entire wavelength range. As stated above, the model includes two kinematic components for every ionization component. The theoretical spectrum is compared with the observed low-state spectrum in Figure 7. The results are very good. In fact, we could not find another combination of models (three or more absorbers) that is significantly superior. Not only does the model provide a good overall fit to many lines of all elements, but it also predicts the strengths of the deep bound-free edges correctly. Thus, the constraints on the 5–7.1 Å silicon and sulphur lines are enough to completely specify a model for the entire spectrum.

3.2.5. Deficiencies in the Modeling

As demonstrated above, the low-state absorption spectrum of NGC 3783 can be satisfactorily explained by our combination of line-of-sight absorbers. The agreement with the observations is very good for all lines with $\lambda < 15$ Å. However, there is a noticeable discrepancy at around 16 Å. At this wavelength range, there are two main sources of opacity: the O vii bound-free continuum (edge at 16.7 Å) and the iron M-shell UTA feature (Behar, Sako, & Kahn 2001). Our photoionization calculations suggest a disagreement between the two in the sense that the strongest iron lines observed are due to ions indicative of a lower level of ionization than that indicated by the strongest oxygen lines observed. Specifically, the peak UTA absorption corresponds to Fe viii–Fe x. For such a level of ionization, our models predict most of the oxygen being in the form of O iii–O vi. However, the observations indicate that most of the oxygen bound-free absorption is due to O vii. The possible origin of this discrepancy is discussed in § 4.

Regarding the spectrum beyond 19 Å, the comparison between the model and the observations is limited by the poorer S/N. While the model shown in Figure 7 is consistent with the data, the predicted depths of several absorption lines in this range (in particular those due to O v and O vi) seem to be stronger than actually observed. This may be a real shortcoming of the model (see comments in § 3.2.4 and in § 4). It may also be the result of the assumed absorption covering factor. As already mentioned, line-profile analysis suggests a mean (over the line profile) covering factor of 0.7–1.0, and all models considered so far assumed the extreme case of an absorption covering factor of unity. The “leakage” of the incident continuum makes little difference at short wavelengths, except for a need to somewhat decrease the assumed Γ . However, leakage can influence the comparison at long wavelengths much more. This is illustrated in Figure 8, which shows a model with $\Gamma = 1.5$ and a line-of-sight covering factor of 0.85. Indeed, the agreement at long wavelengths is much better. The differences between the two assumed slopes and covering factors are well within the model uncertainties.

We have attempted to model the high-state spectrum by assuming the same ionization components and by changing the luminosity and the ionization parameter by the factor inferred from the observed increased luminosity in the short wavelength continuum (~ 1.5). The result is a very poor fit to the long-wavelength continuum luminosity and to the

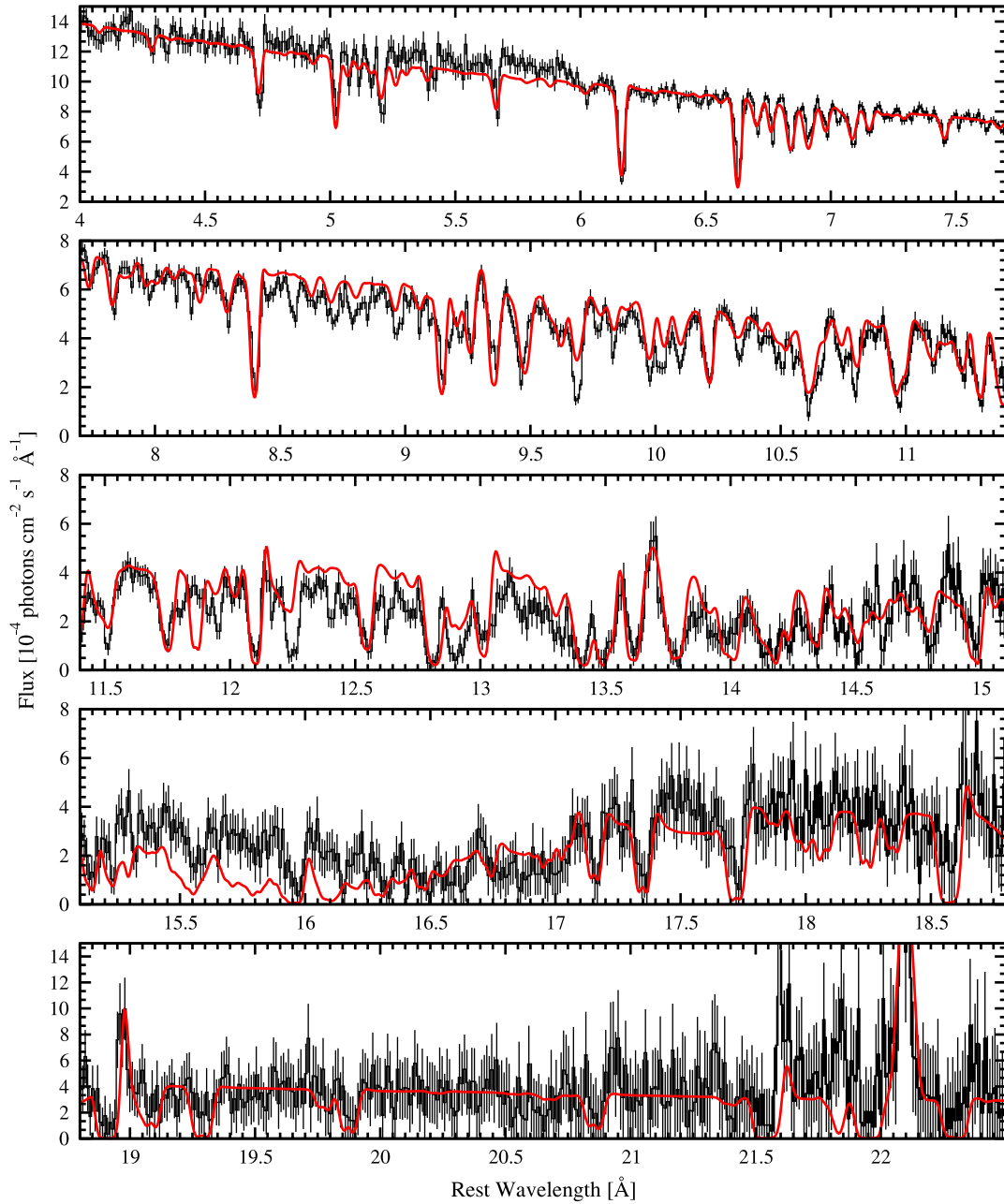


FIG. 7.—Comparison of the low-state spectrum with the six-component model (three ionization components each split into two kinematic components). Note that most of the apparent discrepancy at around 5–6 Å is due to a known calibration problem (H. Marshall 2003, private communication).

intensities of many lines. The reason is that such a small luminosity change results in an opacity change that is too small to account for the very large difference (factor of ~ 4) between the low- and the high-state spectra at long wavelengths. This means that the high- and the low-state spectra are inconsistent with the assumption of a simple response of the gas to continuum luminosity variations.

There is a simple and satisfactory solution for the high-state spectrum that involves the appearance of an additional continuum component. This second, long-wavelength component (sometimes referred to as a “soft excess”) appears only during high state. We have therefore modeled the high-state continuum by two power laws: the low-state power law ($\Gamma = 1.6$) and a steeper component with $\Gamma = 3.2$, which dominates at long wavelengths. We find a satisfactory solu-

tion for the high-state spectrum when the $\Gamma = 3.2$ component emits 40% of the flux of the $\Gamma = 1.6$ component at 12.398 Å (1 keV). (We note that this is not a unique combination, and fits of similar quality can be obtained for other combinations of slope and normalization.) The two continua are shown in Figure 3, along with the high- and the low-state spectra. Given the two component continuum, we find a very good agreement for the high-state line and continuum spectrum by assuming *no opacity variations*. The quality of the fit is similar to the low-state fits shown in Figures 7 and 8.

To further illustrate this point, in Figure 9, we show the high-state spectrum divided by the low-state spectrum (binned to reduce the noise) along with the ratio of the two assumed continua. The diagram shows that any remaining

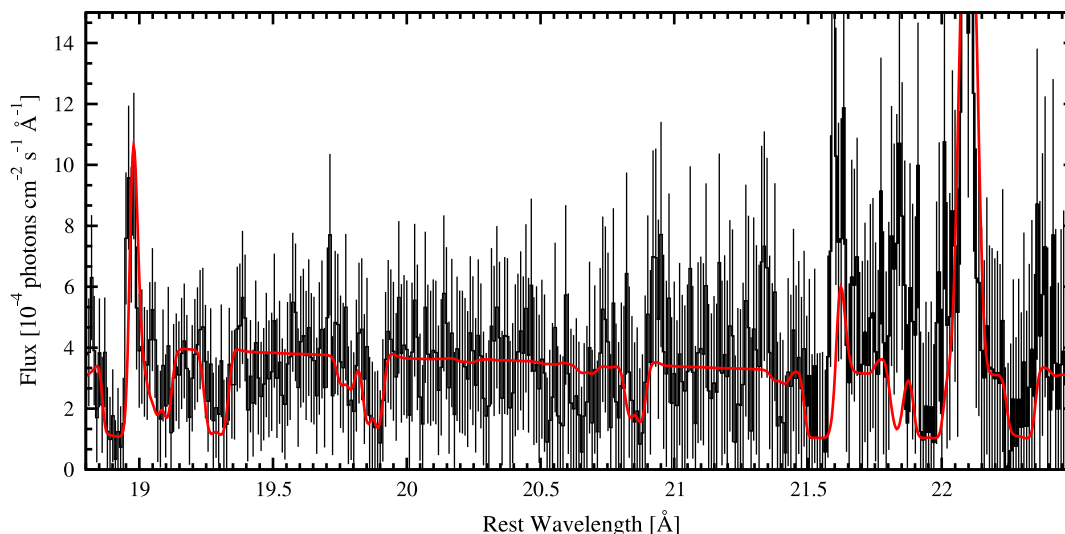


FIG. 8.—Model vs. observation for the long-wavelength spectrum assuming $\Gamma = 1.5$ and a line-of-sight covering factor of 0.85 for all absorbers

spectral features are entirely consistent with the noise. The S/N in this diagram is not high enough to completely rule out some opacity-like variations at long wavelengths. In particular, there is some excess emission near the O VII and O VIII recombination edges that may hint to extra emission in the high-state spectrum. (Note that we do not expect the emission features to disappear by this division.) However, such opacity variations must contribute very little to the spectral variations observed at long wavelengths.

Finally, the emission-line spectrum of NGC 3783 can be explained by assuming X-ray emitters with the same properties found for the ionized absorbers. The emitted line photons are probably observed through the absorber, as indicated by the combined emission-absorption profiles of several resonance lines. The model is problematic at around 21.8 Å, where it fails to reproduce the O VII intercombination emission line. The emission covering factor required is about 0.1 (see § 4.1), consistent with the value of approximately 0.05–0.15 obtained by Behar et al. (2003).

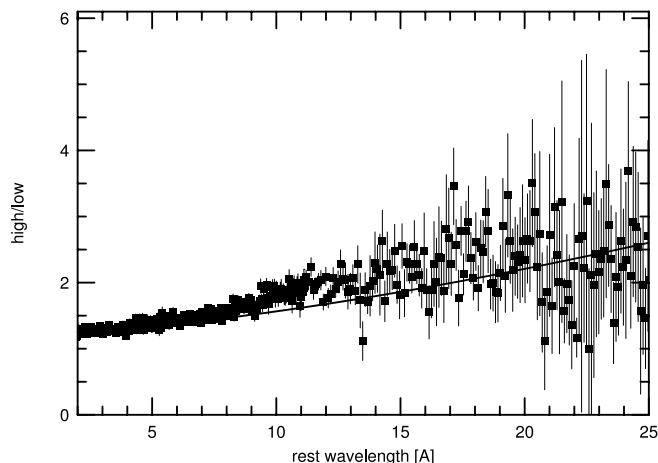


FIG. 9.—Ratio spectrum of NGC 3783: points with error bars are the result of dividing the high-state spectrum by the low-state spectrum. The binning is 0.04 Å for $\lambda < 11$ and 0.1 Å at longer wavelengths. Smooth line: Same division applied to the two continua shown in Fig. 3.

4. DISCUSSION

This section discusses the main results of the new analysis of all the *Chandra* observations of NGC 3783 performed to date.

The main new finding of our work is the large increase in flux between the low and high states, which is *not* accompanied by any significant change in the properties of the absorbers. The central source in NGC 3783 fluctuates between two such flux states on a 20–120 days timescale, and the best description of the observed variations is the appearance and disappearance of a “soft excess,” low-energy continuum component. These lead to important conclusions regarding the nature of the continuum source. Other important conclusions are the multicomponent nature of the absorber and the large range of ionization. Below, we discuss some interpretations.

4.1. Physical Properties of the Absorbing Gas

We found that three ionization components with different properties and a large range of ionization are required to fit the spectrum of NGC 3783. Each of those components is split into two kinematic components, as implied by the observed line profiles reported in Paper 1. The three “generic absorbers” of our model are listed in Table 4 and shown in Figures 5 and 6. As explained above, the number of real components and the exact values of U_{ox} and N are not very meaningful, since several somewhat different combinations of ionization components give equally good fits. Rather, the values chosen here are representative average ionization parameters, and the total column densities

TABLE 4
PARAMETERS OF THE THREE GENERIC MODELS

Model	$\log(U_{\text{ox}})$	$\log(N)$
Low ionization.....	−2.4	21.9
Intermediate ionization.....	−1.2	22.0
High ionization.....	−0.6	22.3

required. Our modeling of the low-state spectrum assumes the underlying X-ray continuum is a single power-law. However, the S/N of the long wavelength spectrum is not high enough to completely rule out the presence of an additional softer continuum component, similar to the one seen during the high states but of much lower luminosity. We also note that there is little (if any) response of the absorbing gas to the short (~ 2 days) timescale continuum variations. Thus, our measurements and model represent some time-averaged spectral properties.

The main difference between the present model and the one given by Kaspi et al. (2001) is the presence of the lowest ionization component. Only the first *Chandra* observation (obtained in 2000 January) was available to Kaspi et al., and hence, was insufficient to reveal the two spectral states. Furthermore, this relatively short observation resulted in the S/N at $\lambda > 18$ Å, which was insufficient to reveal the true shape of the continuum. Hence, Kaspi et al. naturally (but incorrectly) assumed the underlying continuum was a single power law for this high-state spectrum. As a result, their preferred model contained a component with a strong O VII bound-free edge but very little absorption at longer wavelengths (i.e., at $\lambda > 18$ Å, the underlying continuum was “recovered”). Our new observations do not show such a recovery. In fact, the absorption in the long wavelength region is dominated by features of K-shell carbon and nitrogen and L-shell nitrogen and oxygen.

The presence of a lower ionization component is also a key point in the K03 work. In their study they assume two absorbers with $\log(U_{\text{ox}}) = -2.77$ (i.e., a factor of about 2 lower than our lowest ionization component) and $\log(U_{\text{ox}}) = -1.23$ (very similar to our intermediate ionization component). Their fit does not require a third, very ionized component. Our reason for suggesting this highest ionization [$\log(U_{\text{ox}}) = -0.6$] component is based on the fit to the lines of Si XIV, S XV, and S XVI. When this component is not included, the discrepancy in column densities of these ions is a factor of 2–3. Several of the lines of these ions are, in fact, missing from the K03 analysis. Moreover, some of the highest ionization lines are badly saturated (e.g., Si XIV $\lambda 6.18$ Å). Thus, a comparison of the observed and the calculated EWs of those lines, as performed by K03, is not sufficient for evaluating the ionic column densities.

Perhaps the largest observed discrepancy between model and observation is due to absorption by the iron M-shell UTA. This feature has been observed in several other AGNs (Steenbrugge et al. 2003 and references therein) with similar shape and central wavelength. Its smooth shape is due to the large number of absorption lines of many iron ions, and the wavelength of largest absorption is ionization dependent. Our modeling of this spectral region includes all the lines in the Behar et al. (2001) calculations (i.e., not only the shorter published list of lines). The central observed wavelength of the feature in NGC 3783 is at around 16.4 Å, suggesting that most of the contribution is from Fe VIII–Fe X. For the assumed SED, this corresponds to gas whose dominant oxygen ions are O III–O VI. In our modeling, most long wavelength absorption is due to the component with $\log(U_{\text{ox}}) = -2.4$ (Fig. 5). The dominant ions in these components are O VI–O VII and Fe X–Fe XII. This corresponds to peak UTA opacity at around 16.1 Å. As shown in Figure 7, the model fits the observed oxygen lines and continua reasonably well but badly misses the position of the UTA absorption.

We have experimented with various other models to try to eliminate this discrepancy. For example, an overabundance of iron relative to oxygen may decrease the level of ionization of iron due to the increased iron opacity. Experimenting with iron abundance that is three times larger resulted in changes that are not large enough to explain the observed discrepancy. We have also experimented with models that include several low-ionization components instead of the single low- U_{ox} component shown here. This, again, gave very little improvement. It seems that the apparent conflict between the oxygen and iron ionization cannot be resolved by these models and we suggest two alternative explanations.

1. The absorbing gas in NGC 3783 may not be in ionization equilibrium because of its low density and the rapid flux variations on timescales that are shorter than the recombination and ionization timescales. This is probably not very important for the short wavelength flux, since its variability timescale is short and the amplitude not very large. The gas responding to this continuum is probably at some mean level of ionization. This, however, is not the case for the soft excess continuum, which varies on a much longer timescale with a much larger amplitude. This can contribute, significantly, to the ionization of the lower ionization species. Different ions react on different timescales, and the gas may never reach an equilibrium. Since all our models assume steady state gas, they may not be adequate to describe the absorbing gas properties. In particular, the iron and oxygen recombination times may be different enough to result in gas where iron is less ionized or oxygen is more ionized compared to the equilibrium situation. The complicated issue of time-dependent ionization is beyond the scope of this paper.

2. The ionization balance of iron depends critically on low-temperature dielectronic recombination (DR) rates that are not well known for the iron M-shell ions. Experience with L-shell iron ions, whose DR rates have been measured and computed recently (Savin et al. 2002 and references therein) shows that, in almost all cases, the previous low-temperature DR rates were consistently smaller than the newly calculated values. Assuming a similar effect in the M-shell ions, we can envisage a situation where, in the absence of realistic DR rate, the entire ionization balance of iron is shifted toward higher ionization. Thus, more realistic low-temperature DR rates may bring models to better agreement with the observations. We note that low-temperature DR rates are also not available for the magnesium and silicon ions that we have modeled. For some of these ions (Mg VIII and Mg IX), these are probably not very important and for others (the relevant silicon ions) the situation is less clear (D. Savin 2003, private communication; but see also Gu 2003). Nevertheless, since we do obtain good agreement between the calculated EWs of these lines and the EWs of other lines observed in the spectrum, we did not consider changing those rates in the calculations.

It is interesting to note that the K03 model assumes a lower level of ionization for all elements, including iron, and hence provides a better fit to the UTA. However, their lower ionization component fails to fit the Si X and Si XI lines around 6.8 Å. Our model was designed to give a very good fit over the 5–7 Å wavelength range and hence produces a lower quality fit to the UTA feature. Thus, there seem to be no satisfactory solution based on a single low-ionization component that explains all these features.

An interesting and somewhat problematic issue is the abundance of O vi, which can also be clearly observed in the far UV (Gabel et al. 2003a, 2003b). Paper I found even the K α line of O vi undetectable with the current S/N. However, revisiting this measurement more carefully and with more accurate atomic data, we can now detect several O vi lines. From two such lines, both of which are probably saturated, we have obtained a lower limit of $10^{17.0} \text{ cm}^{-2}$ on the column density of O vi. This is much higher than the value ($10^{16.0 \pm 0.3} \text{ cm}^{-2}$) obtained from the *XMM-Newton* RGS spectrum (Behar et al. 2003). Moreover, the values predicted from our model ($10^{17.96} \text{ cm}^{-2}$) are even larger. Such a large value is problematic for several reasons. It may be in contradiction with the UV observations of the source (see below), it is much larger than the values obtained from the RGS observations, and it results in a prediction of a strong absorption line at around 21.87 Å, which is not seen in the spectrum (Fig. 7, the absorption line underneath the O vii intercombination line).

An explanation of the discrepancy between the values for the O vi column density measured by *Chandra* and *XMM-Newton* is the crowded region of the spectrum where O vi K α resides. In particular, the lower spectral resolution of the *XMM-Newton* RGS makes it extremely difficult to resolve the weak O vi absorption line at 22.01 Å in the presence of the bright O vii forbidden emission line (22.10 Å). We also wish to note that with the lack of laboratory measurements for the O vi wavelengths, high-resolution astrophysical spectra such as the present one constitute the best determination of these wavelengths currently available. The *Chandra* data, along with the assumption that O vi is outflowing at the same velocity as O vii, places the O vi K α line at a rest wavelength of 22.01 ± 0.01 Å. This value is in agreement with our model wavelength of 22.005 Å, calculated with the HULLAC atomic code, as well as with the value measured in NGC 5548 (Steenbrugge et al. 2003), but is somewhat different from the value of 22.05 Å calculated by Pradhan (2000) using the R-matrix method. For more information, see Behar & Kahn (2002).

An O vi column density less than 10^{17} cm^{-2} is also inconsistent with theoretical predictions based on modeling the abundances of Mg viii, Si viii, and O vi. This is illustrated in Figure 10, where we show calculations for the fractional abundance of oxygen, silicon, and magnesium ions as a function of U_{ox} , assuming an incident continuum similar to the one used here. The diagram shows the very similar fractional abundance of O vi, Mg viii, and Si viii as a function of ionization parameter. Using the measured EW of the Si viii $\lambda 6.998$ line, which is an unblended, easy-to-measure feature, we can use Figure 10 and the assumed silicon-to-oxygen abundance ratio to derive an estimate for the column density of O vi. This number is very close to the model prediction. The situation is more complicated regarding magnesium, since several of the relevant lines (around 9.4 Å) are blended with neon lines. However, we could obtain an estimate of the EW of the Mg viii $\lambda 9.506, 9.378$ lines that are good enough to constrain the Mg viii column density. The O vi column density based on this measurement is, again, much larger than 10^{17} cm^{-2} and in good agreement with the model prediction.

A comparison with the K03 work shows a disagreement by a factor of 2 in the total (hydrogen) column density of the lowest ionization absorber. One reason for the difference is that K03 analyze the combined (high- and low-state) spec-

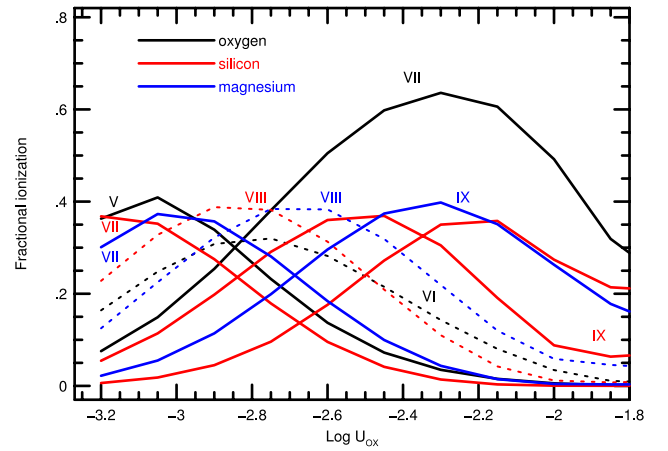


FIG. 10.—Fractional ionization of oxygen, magnesium, and silicon ions in a low-density gas of our chosen composition exposed to the NGC 3783 low-state continuum. Curves: Mean ionization of various ions averaged over a column density of $10^{21.5} \text{ cm}^{-2}$. Note the great similarity in the ionization of O vi, Mg viii, and Si viii (dotted lines).

trum, which is then interpreted in terms of a different amount of bound-free absorption. Another reason is the somewhat larger oxygen abundance assumed by K03 (the oxygen column densities of the low-ionization components in the two papers actually differ only by a factor of 1.35). We also note that the inner-shell O vi lines that we have used to determine the limit on the column density of this ion are missing from the K03 model. This makes a noticeable difference in the spectral fitting at around 21 Å.

Finally, we have looked for the lowest O vi column density allowed by the observations if we remove the constraint imposed by the short wavelength continuum slope (§ 3.2.4) and keep the ionization parameter unchanged. This means finding the lowest column density for the $\log(U_{\text{ox}}) = -2.4$ component, which is still consistent with the measured EWs of the 5–7.1 Å silicon and sulphur lines. We found this limit to be $\log(N) \gtrsim 21.7$ for the low-state spectrum and $\log(N) \gtrsim 21.6$ for the high-state spectrum. These lower limits on the column densities are consistent with the uncertainties given in Table 1. Under these assumptions, the column density of O vi in the low-state spectrum can be as low as $10^{17.76} \text{ cm}^{-2}$. This column is large enough to produce saturated O vi lines at 21.01 and 21.87 Å. It also requires a much harder continuum ($\Gamma = 1.4$).

4.2. Outflow Velocity and Covering Factor

Some of the parameters our model are based on measured profiles of several absorption lines that were shown in Paper I to include at least two components with different outflow velocities. The measurements in Paper I also show that the relative EWs of the two components seem to be ionization independent and that most of the lines used for the profile analysis were heavily saturated. This suggests that the apparent optical depths of those lines are determined by the covering factor rather than the line opacity, and hence, similar to the case seen in many UV absorption systems in AGNs (e.g., Barlow, Hamann, & Sargent 1997; Arav et al. 1999). The covering factor of the lower velocity components of the O vii, Ne x, and Si xiv lines is in the range 0.8–1.0. The covering factor of the larger velocity component of the same

lines, assuming saturated profiles, is 0.6–0.8. We also note that the large number of iron lines near the UTA center gives an independent estimate of the covering factor, which is at least 0.85.

Figure 8 shows that models with a covering factor less than unity provide fits to the data of similar quality. Using the silicon and sulphur lines (as in § 3.2.3), we find three ionization components are again required, each with parameters similar to those listed in Table 4. The only difference is the need to assume a somewhat harder ionizing continuum. The fit to the long wavelength lines is, in fact, somewhat better than that produced by the full covering models. However, given the low S/N at those wavelengths, this is not a strong conclusion. Thus, the data-model comparison cannot constrain the covering factor beyond the actual observations. The most important conclusion is that the covering factor is similar in low- (e.g., O VII and the iron UTA) and in high- (e.g., Si XIV, Ne X) ionization lines.

4.3. Density, Location, and Thermal Stability of the Absorbing Gas

Our measurements and analysis are consistent with no variations in the absorbers' properties on timescales of 1–4 days. There are also indications for no spectral changes over much longer periods, perhaps a few months. For instance, we find no evidence for any significant narrow (<1 Å) spectral features in the high- to low-state spectral ratio shown in Figure 9. The reason we cannot constrain the variability of the absorbers on short timescales are the fast, relatively small amplitude fluctuations in the luminosity of the central source (maximum amplitude of about a factor of 2). As a result of these variability characteristics of the illuminating continuum, the lack of significant spectral variations may be due to the ionization level of the gas reflecting the *time-averaged* ionizing luminosity rather than very long ionization or recombination times. This conclusion, therefore, depends primarily on the direct comparison between the low- and high-state spectra, and thus, on the S/N in the lower quality spectrum used for the comparison (the high-state spectrum).

To further examine this point, we have calculated the theoretical spectrum appropriate for the high-state continuum under the assumption that the absorbing gas responds instantly to changes in the ionizing continuum. This would be the case if the gas along the line-of-sight was of very high density. The initial conditions are those assumed for the low-state continuum, and the change in the SED as described earlier: a two-component X-ray continuum, where the long-wavelength component is assumed to extrapolate down to 40 eV. The increase in flux between the low and high states was assumed to be a factor of 1.5 at 4 Å (see Fig. 3). Figure 11 shows two theoretical spectra: the low-state spectrum (*blue*) is the same model shown in Figure 7, the high-state spectrum (*red*) is the result of these new calculations. The two are clearly different. In particular, the Si VII, Si VIII, and Si IX lines are much weaker for the high-state model. This is because of the large increase in flux at longest wavelengths, with the largest consequences for the lowest ionization component (U_{ox} has increased by a factor close to 2 and U_X by a factor of 6.6). The variations predicted by this theoretical exercise are much larger than those observed (Table 1 and Fig. 4). This illustrates that the gas did not simply react to the differences in the illuminating continuum

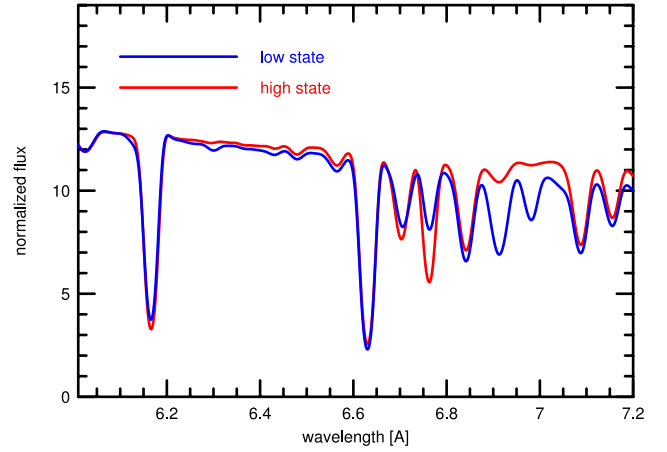


FIG. 11.—Low-state and high-state theoretical spectra, assuming the observed variable NGC 3783 continuum and line-of-sight gas that responds instantly to continuum variations. The low-state model (*blue*) is the one described earlier and shown in Fig. 7. The high-state spectrum (*red*) assumed the high-state SED discussed in the text. Such a continuum results in much weaker Si VIII and Si IX lines.

between the low and high states. An even stronger conclusion is obtained from the fact that at long wavelengths, the differences observed between the two states are much larger than can be explained by simple variations in opacity.

Given the above findings, we can place limits on the electron density (n_e) and the distance from the central source (D) for each absorption component. We used the temperatures derived from the models, average recombination times for the dominant oxygen and silicon ions, and assumed there is no response to continuum variations on a timescale of 10 days. We find $n_e < 5 \times 10^4 \text{ cm}^{-3}$ and $D > 3.2 \text{ pc}$ for the $\log(U_{\text{ox}}) = -2.4$ component, $n_e < 10^5 \text{ cm}^{-3}$ and $D > 0.63 \text{ pc}$ for the $\log(U_{\text{ox}}) = -1.2$ component, and $n_e < 2.5 \times 10^5 \text{ cm}^{-3}$ and $D > 0.18 \text{ pc}$ for the $\log(U_{\text{ox}}) = -0.6$ component. The corresponding masses are $8.1 \times 10^3 C_f$, $390 C_f$ and $64 C_f$ solar masses, respectively, where C_f is the absorption (4π) covering factor. The mass outflow rate is dominated by the lowest ionization component and is approximately $75 C_f \epsilon v_{\text{outflow}} / 500 \text{ km s}^{-1}$ solar masses per year, where ϵ is the radial filling factor of the flow. The very large number suggests a short-duration outburst rather than continuous ejection. We also note that the covering factor can be small, of the order of 0.1. The above distances are in agreement with the findings of Behar et al. (2003), who have suggested the outflow is located at a distance of a few parsecs, and is extended beyond 10 pc based on a comparison between the soft X-ray emission and absorption characteristics of the *XMM-Newton* data.

A significant new aspect of our model is that the product $n_e \times T$ is similar (within a factor of $\lesssim 2$) for all three absorption components. This raises the interesting possibility that all the components are in pressure equilibrium (assuming gas pressure dominates the total pressure, i.e., radiation pressure and turbulent pressure are not important), and they all occupy the same volume of space. To test this idea, we have calculated thermal stability curves $\log(T)$ versus $\log(U_{\text{ox}}/T)$ for the low-state continuum and our assumed composition (Table 2) under various assumptions. We have kept the UV SED unchanged and varied $\Gamma(0.1\text{--}50 \text{ keV})$ over

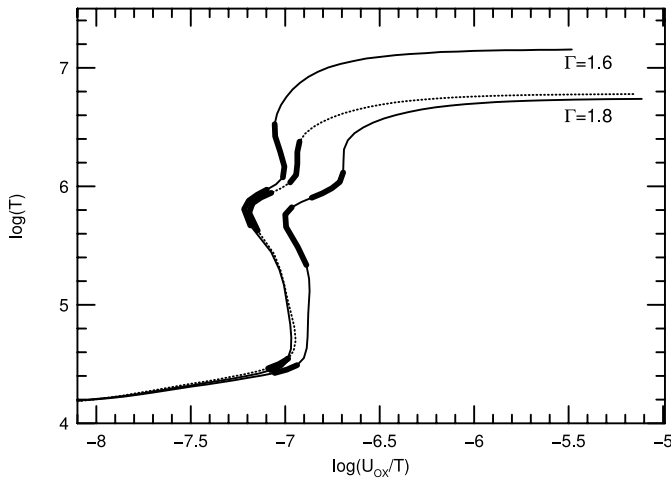


FIG. 12.—Thermal stability curves for a low-density gas exposed to the low-state continuum of NGC 3783. The two curves marked by Γ are for a bare continuum with a 0.1–50 keV slope as marked. *Dotted line*: Stability curve for a gas exposed to the $\Gamma = 1.8$ continuum seen through the $\log(U_{\text{ox}}) = -2.4$ absorber. *Thick sections*: Locations of the three absorbers considered in this work, with the corresponding uncertainties on the ionization parameters. All ionization components considered in this work are situated on thermally stable parts, and they all have roughly the same gas pressure.

a wide range. We have also investigated the possibility of a line-of-sight attenuation by the absorbing gas. This can be relevant for the situation under study since, even in the simplest geometry, two of the absorbers do not have a clear view of the central radiation source. Screening by the lowest ionization component [$\log(U_{\text{ox}}) = -2.4$] is the most important, since this gas modifies the transmitted spectrum much more than the other components (see Fig. 5). Three such stability curves are shown in Figure 12, along with the location of the three ionization components. The exact location depends on the details of the assumed SED, the gas metallicity, and opacity.

The interesting feature of the stability diagram is that all radiation fields considered here result in extended, almost vertical parts between $T \simeq 3 \times 10^4$ and 2×10^6 K. The curve for $\Gamma = 1.6$ has a more extended vertical part, since the higher mean energy of the radiation field results in a Compton temperature. Screening by the lowest ionization component in NGC 3783 is indeed important but does not change the main result that, given the uncertainties on the SED and composition, all three ionization components lie on the stable part of the curve. We also note that, while here we only considered gas with a single composition, the details of the stability curve are abundance dependent. Needless to say, very different curves will be obtained for significantly different SEDs.

We note that K03 reach similar conclusions regarding the pressure equilibrium of their two ionization components. However, in our model, all components are situated on stable branches of the thermal stability curve (Fig. 12), while according to K03, their high-ionization component is situated on the unstable branch (their Fig. 16). We suspect that the difference is due, in part, to the different SED and metallicity assumed by K03, and due, in part, to the method they used to calculate the curve.

The existence of an additional stable region along the curve of thermal equilibrium (intermediate between the cold

and the hot branches) where “warm” (few $\times 10^5$ K) can survive is not a new idea. It has been discussed by Marshall et al. (1993) in their study of the multiphase medium in NGC 1068 and later by many others. Reynolds & Fabian (1995) discussed the stability criteria and noted the narrow range of ionization parameter allowed for warm absorbers. Hess, Kahn, & Paerels (1997) discussed the various parameters governing the stability curve (metallicity and more). Komossa and collaborators (e.g., Komossa & Fink 1997; Komossa & Meerschweigen 2000) calculated many such curves for different SEDs and metallicities and discussed the location of warm absorbers as well as the possible link between the narrow-line region and the X-ray gas. Krolik & Kriss (2001) considered multiphase, warm-absorber winds and noted the various locations of stable, overheated and overcooled gas. Kinkhabwala et al. (2002) revisited the thermal stability issue in NGC 1068 and showed that a wide range of U_{ox} is needed to account for the observed X-ray emission lines. Chelouche & Netzer (2003) investigated the changes in the stability criteria for clouds with large internal line radiation pressure.

Most of these earlier works focused either on the allowed parts of the curve from general stability conditions or on the location of a certain absorber observed in a certain source. Our work shows that three very different absorbers in a source can all occupy extended, stable parts of the curve where the gas pressure is roughly the same. This means there may well be more than three absorbers spread over the vertical branch of the curves in Figure 12. The three ionization parameters considered here may therefore represent some volume-averaged properties of the entire cloud ensemble. The column densities are therefore the total column densities of a large number of such clouds. Moreover, the most ionized component may provide the confining medium for the two other ionization components. Needless to say, real confined outflowing clouds are characterized by a more complicated density and pressure structure than with the simplified, constant density clouds considered here (e.g., see Chelouche & Netzer 2001).

The pressure equilibrium between all three absorbers in NGC 3783 suggest they occupy the same general location. This allows additional constraints to be placed on their density and location. Specifically, we require that the distance of this region is at least 3.2 pc (the minimum distance of the lowest ionization component). However, this zone cannot be much further away because of total size and volume considerations. Under the assumed conditions, the highest ionization parameter component has the lowest density, and hence, the largest dimension. However, its radial extent cannot exceed about 500 pc (the approximate radius of the narrow-line region), and thus, its mean density cannot fall below about 10 cm^{-3} . Pressure equilibrium then dictates the density of the lowest ionization component and a maximum distance of about 25 pc. This limitation is only imposed on discrete clouds—i.e., on the mean properties of the gas. Real absorbers may not be “clouds;” they can cover a large range of distances and can have properties that depend on location. The detailed investigation of such models is beyond the scope of the present paper.

4.4. The Emission Lines

There is no indication for flux variation in any of the observed emission lines. However, the measurement

uncertainty on these line is rather large, since the strongest lines are observed at the long wavelengths where the S/N is poor. We obtain satisfactory fits for most lines by assuming that the emission-line gas has the same column density and ionization parameter as the absorbing gas. The covering factors required for the emitting gas are 0.2–0.3 for the $\log(U_{\text{ox}}) = -2.4$ component, 0.1–0.2 for the $\log(U_{\text{ox}}) = -1.2$ component, and ~ 0.1 for the $\log(U_{\text{ox}}) = -0.6$ component. The large range is due to the uncertainties in the continuum placement and in estimating the fraction of the O VII and O VIII emission lines that are being absorbed by the line-of-sight gas. (The model shown in Figs. 7 and 8 assumes that *all* the emitted photons are seen through the absorbers.)

A clear shortcoming of the model is the fitting of the intercombination O VII line. The intensity predicted for this line is too small by a large factor (2–4). A large part of the discrepancy is due to the O VI $\lambda 21.87$ Å absorption line situated close to this emission (Fig. 7). This may be related to the O VI problem discussed earlier. Alternatively, it may be a consequence of our assumption that all emission-line photons are seen through the absorbers. Indeed, a model that assumes no absorption of the emitted photons by the line-of-sight gas (not shown here) would give a much better agreement to the O VII absorption complex. This would also require a smaller emission covering factor. Obviously, we cannot determine the exact geometry using current observations, and the real case may well be intermediate between those two extremes.

We also note on the difference between the absorption covering factor (0.8–1.0) and the emission covering factor (0.1–0.3). Given the uncertain geometry and the fact that the first is a line-of-sight covering factor and the second a global (4π) property, the two are perhaps consistent with each other. We did not investigate all possibilities and cannot comment in detail on special cases like biconical flows or a torus geometry (e.g., Krolik & Kriss 2001).

Finally, comparing our method with that of K03, we note that those authors do not calculate the emission line flux and profile in a self-consistent way. Instead, they add Gaussian-shaped emission profiles to their calculated absorption profiles (e.g., their Fig. 6). This can result in significant differences regarding the line flux and EW. For example, our default approach assumes that all emission lines are seen through the absorber. In such a case, the entire “blue” wing of many emission lines is absorbed. Clearly, this affects the EW of the emission lines but has almost no effect on the EW of the absorption features. In contrast, the approach adopted in K03 always results in a decrease of the EW of the absorption lines.

4.5. UV Absorbers in NGC 3783

NGC 3783 contains time-variable absorbers in the UV that have been described in various earlier publications (Gabel et al. 2003a and references therein). Our analysis clearly indicates that at least one X-ray component contains gas which is of sufficiently low ionization so as to produce strong absorption lines of C IV, N V, and O VI in the UV.

The predicted EWs of these UV lines depend on two factors that have been given little attention in this work: the exact shape of the UV continuum and the covering factor appropriate for the UV absorbers. A UV continuum that is softer than that assumed here can result in higher levels of ionization for carbon, nitrogen, and oxygen, with little effect

on most X-ray lines. This is very important for the C IV $\lambda 1549$ and N V $\lambda 1240$ Å lines, but less so for the UV lines of O VI that are directly linked to the O VI column density discussed here.

As for the covering factors, the size of the UV continuum source is likely to be much larger than the size of the central X-ray source. Thus, the covering factor appropriate in the UV can be different to that appropriate in the X-ray. This will result in saturated UV absorption lines whose EWs are smaller than the ones indicated by the column densities derived here. However, our upper limit on the density of the low-ionization component, combined with its column density, suggests a very large line-of-sight dimension ($>10^{17}$ cm). Assuming lateral dimension of the same size or larger, we conclude that the physical dimension of this component is much larger than the expected dimension of any likely UV source (e.g., the surface of a thin accretion disk). A combined analysis of the UV and X-ray results, taking these such points into consideration, is in progress.

UV absorbers are also UV emitters, and the low-ionization component can also contribute to the observed UV emission lines. Our photoionization calculations show that this contribution is very small. For example, an emission covering factor of 0.1, similar to the one deduced from the X-ray emission lines, will produce an O VI $\lambda 1035$ line with emission EW of about 1 Å.

4.6. The Long Wavelength Component

Perhaps the most interesting result of this study is the appearance and disappearance of the soft excess component. This broadband continuum source was seen in two of the six observations. On average, these are the two observations with the highest luminosity. An increase in softness ratio with increasing source luminosity is well known and well documented in a number of AGNs (e.g., Magdziarz et al. 1998; Chiang et al. 2000; Markowitz & Edelson 2001). However, we are not aware of a softness ratio increase that is *not correlated* with a short wavelength flux increase. NGC 3783 seems to be the first AGN to show this phenomenon, but we suspect that careful spectroscopic monitoring will reveal the same or a similar behavior in other sources. This has important consequences to the continuum production mechanism as well as for the modeling of the warm X-ray gas around the center.

We do not know the origin of the soft continuum source. In particular, we do not have information on its flux at wavelengths $\lambda > 30$ Å (the source was not in a high state in any of the published *XMM-Newton* observations). It may be related to a broadband phenomenon (e.g., due to a flaring accretion disk) or a component covering a narrower band (e.g., a single-temperature blackbody). Simple global energy consideration shows that this phenomenon is unrelated to the appearance of broad emission features like those claimed to be seen in at least two sources and interpreted as due to relativistic disk lines (Branduardi et al 2001; Mason et al. 2003; but see also Lee et al. 2001).

Finally, we must comment on the possibility of a more complex behavior. Our analysis is based on the fitting of a single power-law continuum at low state and the addition of a soft X-ray component during the high state. However, an equivalent analysis could be carried out in the reverse order—i.e., starting from a pure power law for the high state and *subtracting* a continuum component to explain the

low-state spectrum. However, as argued earlier, the observed spectral changes at long wavelengths are too large to be explained by pure opacity variations, and it is not at all clear what other mechanism could explain an AGN continuum with a flux deficit at long wavelengths.

5. CONCLUSIONS

Our detailed measurements and analysis of the 900 ks data set of NGC 3783 lead to the following results:

1. The source fluctuates in luminosity, by a factor of ~ 1.5 , during individual 170 ks observations. The fluctuations are not associated with significant spectral variations.

2. On timescales of 20–120 days, the source exhibits two very different spectral shapes denoted here as the high and low states. The two are associated with different softness ratios that seem unrelated to the total X-ray luminosity. The observed changes in the underlying continuum can be described as due to the appearance (in the high state) and disappearance (in the low state) of a soft excess component. The origin of this continuum component is not clear. To the best of our knowledge, NGC 3783 is the first AGN to show such a behavior.

3. The appearance of the soft continuum component can explain all spectral variations observed within the measurement uncertainties. There is no need to invoke opacity changes between the high and low states. This conclusion depends mostly on the S/N in the high-state spectrum.

4. A combination of three ionization components, each split into two kinematic components, provides a good description of the intensity of almost all the absorption lines

and bound-free edges observed. The components span a large range of ionization and have a total column of about $4 \times 10^{22} \text{ cm}^{-2}$. The only real discrepancy between the observed and theoretical spectra are for the iron M-shell UTA feature at 16–16.5 Å. This is most likely due to inadequate dielectronic recombination rates currently available to use in our calculations. The largest other uncertainty is in the column density of O VI.

5. The three generic absorbers discussed in this work have very similar values of $n_e \times T$. We speculate that the absorbers may be in pressure equilibrium with each other, occupying the same volume in the nucleus. This is the first confirmation of the location of several X-ray absorbers on the vertical part of the $\log(T)$ versus $\log(U_{\text{ox}}/T)$ stability curve of an AGN.

6. We have obtained three lower limits on the gas distance from the center, corresponding to our three generic absorbers. The limits are 3.2, 0.6, and about 0.2 pc for the low-ionization, intermediate-ionization, and high-ionization absorbers, respectively. The pressure equilibrium assumption implies distances in the range 3–25 pc.

This work is supported by Israel Science Foundation grant 545/00. H. N. thanks S. Kahn and the astrophysics group at Columbia University for hospitality and support during a summer visit in 2002. E. B. was supported by the Yigal-Alon Fellowship and by the GIF Foundation under grant 2028-1093.7/2001. We gratefully acknowledge the financial support of CXC grant GO1-2103 (S. K., W. N. B., and I. M. G.), NASA LTSA grant NAG 5-13035 (W. N. B.), and the Alfred P. Sloan Foundation (W. N. B.).

REFERENCES

- Arav, N., Becker, R. H., Laurent-Muehleisen, S. A., Gregg, M. D., White, R. L., Brotherton, M. S., & de Kool, M. 1999, *ApJ*, 524, 566
- Barlow, T. A., Hamann, F., & Sargent, W. L. W. 1997, *ASP Conf. Ser.* 128, *Mass Ejection from Active Galactic Nuclei*, ed. N. Arav, I. Shlosman, & R. J. Weymann (San Francisco: ASP), 13
- Behar, E., & Kahn, S. M. 2002, *NASA Laboratory Astrophysics Workshop*, preprint (astro-ph/0210280)
- Behar, E., & Netzer, H. 2002, *ApJ*, 570, 165
- Behar, E., Sako, M., & Kahn, S. M. 2001, *ApJ*, 563, 497
- Behar, E., et al. 2003, *ApJ*, 598, 232
- Blustin, A. J., Branduardi-Raymont, G., Behar, E., Kaastra, J. S., Kahn, S. M., Page, M. J., Sako, M., & Steenbrugge, K. C. 2002, *A&A*, 392, 453
- Branduardi-Raymont, G., Sako, M., Kahn, S. M., Brinkman, A. C., Kaastra, J. S., & Page, M. J. 2001, *A&A*, 365, L140
- Chelouche, D., & Netzer, H. 2001, *MNRAS*, 326, 916
- . 2003, *MNRAS*, 344, 223
- Chiang, J., Reynolds, C. S., Blaes, O. M., Nowak, M. A., Murray, N., Madejski, G., Marshall, H. L., & Magdziarz, P. 2000, *ApJ*, 528, 292
- Gabel, J. R., et al. 2003a, *ApJ*, 583, 178
- . 2003b, *ApJ*, 595, 120
- George, I. M., Turner, T. J., Mushotzky, R., Nandra, K., & Netzer, H. 1998, *ApJ*, 503, 174
- Gu, M. F. 2003, *ApJ*, 589, 1085
- Hess, C. J., Kahn, S. M., & Paerels, F. B. S. 1997, *ApJ*, 478, 94
- Kaspi, S., Brandt, W. N., Netzer, H., Sambruna, R., Chartas, G., Garmire, G. P., & Nousek, J. A. 2001, *ApJ*, 554, 216
- . 2002, *ApJ*, 574, 643 (Paper I)
- Kinkhabwala, A., et al. 2002, *ApJ*, 575, 732
- Komossa, S., & Fink, H. 1997, *A&A*, 322, 719
- Komossa, S., & Meerschweinchen, J. 2000, *A&A*, 354, 411
- Krolik, J. H., & Kriss, G. A. 2001, *ApJ*, 561, 684
- Krongold, Y., Nicastro, F., Brickhouse, N. S., Elvis, M., Liedahl, D. A., & Mathur, S. 2003, *ApJ*, 597, 832 (K03)
- Lee, J. C., Ogle, P. M., Canizares, C. R., Marshall, H. L., Schulz, N. S., Morales, R., Fabian, A. C., & Iwasawa, K. 2001, *ApJ*, 554, L13
- Magdziarz, P., Blaes, O. M., Zdziarski, A. A., Johnson, W. N., & Smith, D. A. 1998, *MNRAS*, 301, 179
- Markowitz, A., & Edelson, R. 2001, *ApJ*, 547, 684
- Marshall, F. E., et al. 1993, *ApJ*, 405, 168
- Mason, K. O., et al. 2003, *ApJ*, 582, 95
- Mathur, S., Elvis, M., & Wilkes, B. 1995, *ApJ*, 452, 230
- Netzer, H. 1996, *ApJ*, 473, 781
- Netzer, H., Chelouche, D., George, I. M., Turner, T. J., Crenshaw, D. M., Kraemer, S. B., & Nandra, K. 2002, *ApJ*, 571, 256
- Pradhan, A. K. 2000, *ApJ*, 545, L165
- Reynolds, C. S., & Fabian, A. C. 1995, *MNRAS*, 273, 1167
- Savin, D. W., et al. 2002, *ApJ*, 576, 1098
- Steenbrugge, K. C., et al. 2003, *A&A*, 402, 477